The Astronomical Journal, 138:963–974, 2009 September doi:10.1088/0004-6256/138/3/963

THE DISTANCE TO NGC 2264

Eric J. Baxter[1], Kevin R. Covey[2], August A. Muench[2], Gábor Fűrész[2], Luisa Rebull[3], and Andrew H. Szentgyorgyi[2]
[1] Astronomy and Astrophysics Department, University of Chicago, Chicago, IL 60637, USA
[2] Harvard Smithsonian Center for Astrophysics, 60 Garden St., Cambridge, MA 02138, USA
[3] Spitzer Science Center, M/S 220-6, 1200 E. California Blvd., Pasadena, CA 91125, USA
Received 2008 September 26; accepted 2009 July 1; published 2009 August 14

ABSTRACT

We determine the distance to the open cluster NGC 2264 using a statistical analysis of cluster member inclinations. We derive distance-dependent values of $\sin i$ (where i is the inclination angle) for 97 stars in NGC 2264 from the rotation periods, luminosities, effective temperatures, and projected equatorial rotation velocities, $v \sin i$, measured for these stars. We have measured 96 of the $v \sin i$ values in our sample by analyzing high-resolution spectra with a cross-correlation technique. We model the observed distribution of $\sin i$ for the cluster by assuming that member stars have random axial orientations and by adopting prescriptions for the measurement errors in our sample. By adjusting the distance assumed in the observed $\sin i$ distribution until it matches the modeled distribution, we obtain a best-fit distance for the cluster. We find the data to be consistent with a distance to NGC 2264 of 913 pc. Quantitative tests of our analysis reveal uncertainties of 40 and 110 pc due to sampling and systematic effects, respectively. This distance estimate suggests a revised age for the cluster of ∼1.5 Myr, although more detailed investigations of the full cluster membership are required to draw strong conclusions.

Key words: methods: statistical – open clusters and associations: individual (NGC 2264) – stars: distances – stars: formation – stars: rotation

1. INTRODUCTION

NGC 2264 is an open cluster in the Monoceros OB1 association containing a large population of young stars. The cluster has been the focus of a number of studies of early stellar evolution dating back to the work of Herbig (1954). NGC 2264 is an ideal target for such studies because of its low line-of-sight extinction and minimal optical nebular emission (Park et al. 2000). In addition, most background stars are obscured from the cluster by the presence of a large molecular cloud complex (Herbig 1954).

Previous distance determinations for NGC 2264 have favored a distance of 800 pc, although there has been considerable spread around this value: 800 pc by Walker (1956), 760 pc by Sung et al. (1997), 760–950 pc by Flaccomio et al. (1999), and 750 pc by Mayne & Naylor (2008); see Dahm (2008) for a complete summary of previous distance measurements. These distance estimates have been primarily derived by fitting empirically or theoretically defined main sequences to the location of high mass (B and A type) stars in the HR diagram. Although extensive Stromgren narrowband photometry is available in the literature (Strom et al. 1971; Perez et al. 1989), it has not yet been used to refine distances to these early type stars (e.g., Anthony-Twarog 1982).

An improved distance estimate to NGC 2264 would lower the uncertainties in the luminosities derived for cluster members, which in turn constrain the cluster's age. As one of the premiere laboratories for studying star formation in the Milky Way, a better estimate of the age of NGC 2264 would further our understanding of processes relevant to early stellar evolution such as angular momentum transfer and the lifetime of circumstellar disks.

In this paper, we determine the distance to NGC 2264 using a statistical technique that relies on measured projected rotation velocities, rotation periods, luminosities, and effective temperatures of the low mass K and M type cluster members. The technique was first developed by Hendry et al. (1993) and has subsequently been used to find distances to the Pleiades, the Taurus star-forming region, and the Orion Nebula Cluster (O'Dell et al. 1994; Preibisch & Smith 1997; Jeffries 2007). This method has the advantage of being nearly independent of stellar evolutionary models.

1.1. The Method

In brief, we first measure the projected rotational velocities of cluster members, $v \sin i$ (where v is the tangential velocity of the stellar surface at the equator and i is the inclination of the stellar rotational axis on the sky such that $i = 90°$ implies an edge-on orientation and $i = 0°$ implies a pole on orientation) from existing high-resolution spectra of NGC 2264 members (Fűrész et al. 2006). An effective temperature, $T_{\rm eff}$, is estimated for each star from either its spectral type or dereddened photometry. Luminosities, L, are estimated for cluster members from measured magnitudes by assuming a nominal value for the cluster distance, a prescription for the cluster reddening, and a standard bolometric correction. Stellar radii are then calculated from the estimated luminosities and effective temperatures using the Stefan–Boltzmann relation. The final data needed for the distance determination are rotation periods obtained from fits to periodic variations in the stellar light curves.

Bringing all of these data together, we calculate $\sin i$ for each star as

$$\sin i = \frac{P \cdot (v \sin i)}{2\pi R_D}, \quad (1)$$

where P is the measured rotation period and R_D is the stellar radius (the subscript indicates that the measured radius is dependent on the stellar luminosity, which depends on the assumed cluster distance, D).

Equation (1) allows us to generate an observed distribution of $\sin i$ that is dependent on the adopted cluster distance. We then model the distribution of $\sin i$ assuming that the rotational axes of stars in the cluster are randomly oriented. By scaling

the input cluster distance so that the observed $\sin i$ distribution matches the predicted distribution, we obtain an estimate for the true cluster distance.

We begin in Section 2 with a description of the data used to determine the distance to NGC 2264; Section 3 describes our measurement of projected rotation velocities by applying a cross-correlation routine to high-resolution spectra of cluster members; Section 4 describes the distance determination technique in detail; our results are discussed in Section 4.6.

2. DATA

As described above, our distance measurement relies on $\sin i$ values for stars in NGC 2264. Four types of data are needed to calculate $\sin i$ for an individual star using Equation (1): the star's period, luminosity, effective temperature, and projected equatorial rotational velocity, $v \sin i$. Period (Section 2.1), effective temperature (Section 2.2), and luminosity (Section 2.3) data were obtained from a catalog compiled by Rebull et al. (2006) and are briefly described below. Most of the $v \sin i$ data, on the other hand, were calculated from spectra (Section 2.4) using a cross-correlation technique further discussed in Section 3.

2.1. Periods

Rotation periods for pre-main-sequence stars are determined by measuring periodic variations in the objects' brightness. These variations arise from the presence of large ($\sim 40^\circ$ angular radius) starspots on the surfaces of these young, magnetically active stars (Herbst 1989). The transit of the starspot(s) as the star rotates diminishes the observed stellar luminosity on the order of a few tenths of a magnitude. This variation is quite stable and can be used to derive precise periods.

Rebull et al. (2006) compiled periods measured for members of NGC 2264 by Rebull et al. (2002), Makidon et al. (2004), and Lamm et al. (2005). The period measurements range from roughly 0.5 to 29 days and are predicted to be accurate to roughly $\delta P/P \approx 1\%$.

2.2. Effective Temperatures

The catalog assembled by Rebull et al. (2006) includes $T_{\rm eff}$ estimates derived from low-resolution spectral types and from the stars' optical colors using the $V-I$ versus $T_{\rm eff}$ relation presented by Hillenbrand (1997). Each star's $V-I$ color was dereddened prior to this calculation as described by Rebull et al. (2002): stars with spectra were dereddened so that their observed $R-I$ colors matched the intrinsic colors of that spectral type on the zero-age main sequence (ZAMS) defined by Bessell (1991), Leggett (1992), and Leggett et al. (1998). The $V-I$ colors for stars without spectra were dereddened assuming the modal reddening of members with measured spectral types. While the use of an overall reddening for the cluster is less than ideal, out of a total of 97 stars for which we derive $\sin i$ values, only 14 lack spectral types. Thus, larger errors associated with photometric based $T_{\rm eff}$ measurements likely have a negligible effect on our results.

T Tauri stars almost certainly do not have a single photospheric temperature; however, observations of the weak T Tauri star V410 by Herbst (1989) indicated the presence of two large, polar starspots with characteristic temperatures of 3100 K, in contrast to the star's 4400 K. photosphere. Observations of larger ensembles of T Tauri stars indicate similar photospheric–spot temperature differentials, and typical spot covering fractions of $\sim$10% (Bouvier & Bertout 1989; Johns-Krull & Gafford 2002).

Somewhat counterintuitively, however, starspots are unlikely to introduce large errors in a star's derived photospheric temperature, particularly for large spot–photosphere temperature differentials. The star's integrated emission is dominated by non-spotted photospheric flux, as the cooler spots emit significantly less flux per unit area. Observational confirmation of this effect was provided by Frasca et al. (2005), who constructed detailed starspot models of RS CVn systems to reproduce broadband photometric light curves and temperature sensitive line ratios from temporally resolved, high-resolution spectra of RS CVn systems. While the best-fit models identified by Frasca et al. (2005) possessed photosphere–spot temperature differentials of $\sim$1000 K, the temperature sensitive spectroscopic line ratios only departed from the photospheric value by $\sim$150 K over the course of the observations.

In their Appendix A, Frasca et al. (2005) outline a formalism for calculating the mean temperature observed from a star with a given spot covering fraction and photosphere–spot temperature differential. Using this formalism, we calculated the difference between a T Tauri star's true (non-spotted) photospheric temperature and the temperature that would be measured from its integrated (spot + photosphere) spectrum. For typical T Tauri star parameters ($T_{\rm phot} = 4000$ K; $T_{\rm spot} = 3200$ K; $f_{\rm spot} = 0.1$), the temperature measured from the combined spot +photosphere I-band spectrum would be 3992 K, only 8 K different from the "true" photospheric temperature.

Given the small size of this effect, we assume that the uncertainties in our derived temperatures are dominated by errors in the observed colors, spectral types, and reddening corrections. We expect that the temperature uncertainties introduced by these effects are roughly $\delta T_{\rm eff}/T_{\rm eff} \approx 5\%$.

2.3. Luminosities

Rebull et al. (2006) calculated luminosities for cluster members from dereddened photometry, assuming a distance to the cluster of 760 pc. Stars without previously determined spectral types were dereddened by the modal reddening value determined for stars with spectral types. Not taking into account the uncertainty associated with the distance assumption, the observed luminosities are likely accurate to within $\delta L/L \approx 35\%$. This estimate includes contributions from uncertainties in spectral type, extinction values, and uncertainty due to source variability (Hartmann 2001).

We note that the luminosity we calculate for each star from its measured photospheric temperature will likely be a slight overestimate, as some fraction of the star's surface will be covered with cooler, less luminous starspots. Again using the formalism presented by Frasca et al. (2005) in their Appendix A, we calculated the expected scale of this effect. For our typical T Tauri star, the bolometric luminosity calculated assuming a single measured photospheric temperature (i.e., $T_{\rm obs} = 3992$ K) is 5% larger than the true luminosity assuming the correct spot–photosphere differential and covering fraction. As the scale of this effect is well within our errors, and as we lack a robust characterization of the spot properties for the stars in our sample, we simply adopt the luminosity implied by the single temperature associated with each star's spectral type.

2.4. Echelle Spectra

Spectra for 923 stars in and around NGC 2264 were obtained from the sample observed by Fűrész et al. (2006) using Hectochelle (Szentgyorgyi 2006), a multiobject echelle spectrograph located on the 6.5 m Multiple Mirror Telescope (MMT).

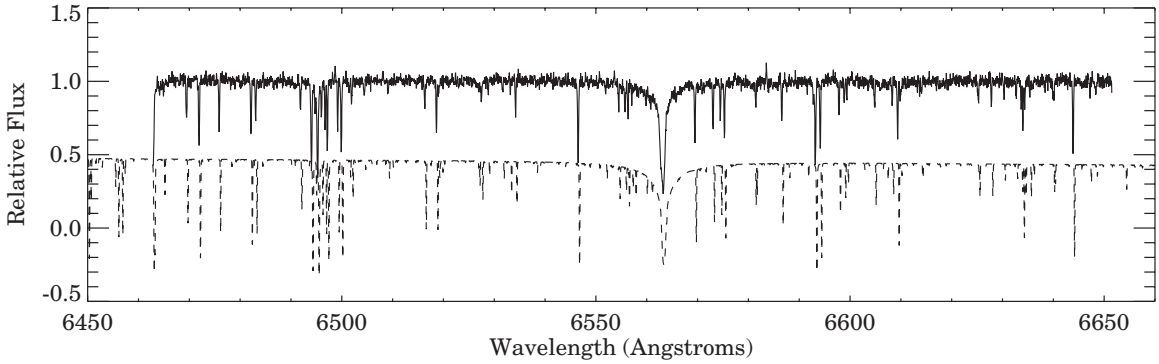

Figure 1. Spectrum of a typical star in our sample (solid line). Also plotted (dashed line) is the best-fitting template spectrum for this star (see Section 3.2). The template spectrum has been shifted to lower flux values for visual clarity. As noted in the text (Section 3.3) the Hα region (from 6545 Å to 6585 Å) was excluded from the cross-correlation procedure because of its strong variability between spectra.

The spectra cover a wavelength range of 6450–6650 Å and have a resolution of $R \sim 34,000$, providing velocity resolution of $\sim$9 km s^{-1}. A typical spectrum obtained for a star in NGC 2264 is shown in Figure 1.

3. PROJECTED ROTATIONAL VELOCITIES

3.1. The Correlation Technique

Because few stars in our initial catalog had previously measured $v \sin i$'s, it was necessary to extract this data from the spectra of Fűrész et al. (2006). To make this measurement, we used a cross-correlation technique similar to that developed by Tonry & Davis (1979). The correlation parameter, $C(v_R)$, between a target (i.e., a cluster member) and a well-matched template spectrum is determined as a function of the radial velocity of the template spectrum, v_R. $C(v_R)$ is obtained by inverse Fourier transforming the product of the discrete Fourier transforms of the target and template spectra (Hartmann et al. 1986). To generate $C(v_R)$, we have developed a custom cross-correlation routine in IDL based on a heavily modified version of a routine originally developed by White et al. (2007).

The location of the peak of $C(v_R)$ corresponds to the value of v_R for which the target and template spectra are best matched. Thus, the correlation procedure provides us with a measure of v_R for stars in our sample. Furthermore, because rotational broadening of the target star's spectral lines results in a broader $C(v_R)$ peak, the width of the $C(v_R)$ peak, σ_C, provides a measure of $v \sin i$ for the target star. The correlation function $C(v_R)$ resulting from cross-correlating one of our target spectra with a template spectrum is shown in Figure 2.

The accuracy of the kinematic properties measured by the cross-correlation technique depends on the quality of the agreement between the strength and shape of the spectral features present in the template and target spectra. To ensure that the target and template spectra are reasonably well matched, we correlate each target spectrum against a grid of template spectra covering a range of temperatures and surface gravities (see Section 3.2). The best matching template is then used to derive $v \sin i$ for that target. The degree of "matching" between a template spectrum and a target spectrum is quantified with a statistical quantity, R, defined as the ratio of the height of the maximum peak in $C(v_R)$ to the root mean square of the anti-symmetric component of $C(v_R)$ (Tonry & Davis 1979). In an idealized scenario in which the target spectrum has no noise, the correlation function would be perfectly symmetric around some particular value of v_R. R therefore measures the strength of the correlation function peak against the noise in $C(v_R)$. Thus, the template that produces the largest R value when correlated against a particular target can be said to be the optimal template for that target.

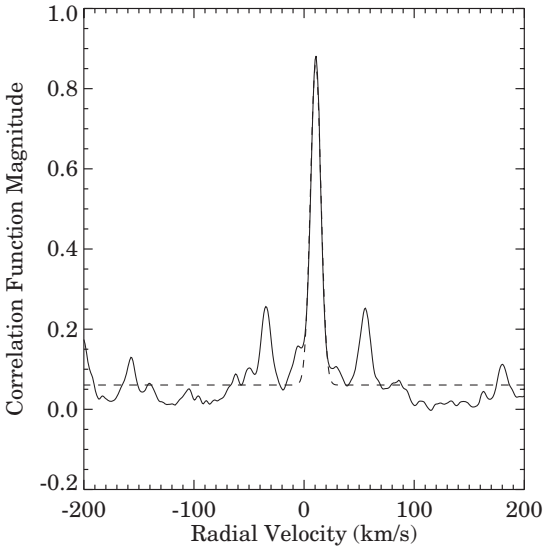

Figure 2. Cross-correlation function resulting from the correlation of a target spectrum with the corresponding best-fit template model. The cross-correlation function shows a clear peak at roughly 10 km s^{-1}; the width of the function formally implies a rotation velocity of about 3.4 km s^{-1}, below our threshold for confident $v \sin i$ detections. A Gaussian fit to the cross-correlation function is shown as a dashed line. The above example represents a better than average cross-correlation result, with an R value of approximately 44.

3.2. The Template Grid

We cross-correlated our targets against a set of templates calculated by Coelho et al. (2005). The template grid covers temperatures ranging from 3000 K to 7000 K in increments of 250 K and $\log g$ (surface gravity) values ranging from 0.0 to 5.0 in increments of 0.5. Because the strength of the Hα line at 6562 Å exhibits strong dependence on accretion that could potentially interfere with our ability to derive $v \sin i$ values, each spectrum was divided into two regions bracketing Hα (a "blue" region at wavelengths below 6545 Å and a "red" region at wavelengths greater than 6585 Å). Both regions were then correlated separately with the template spectra. Subsequent

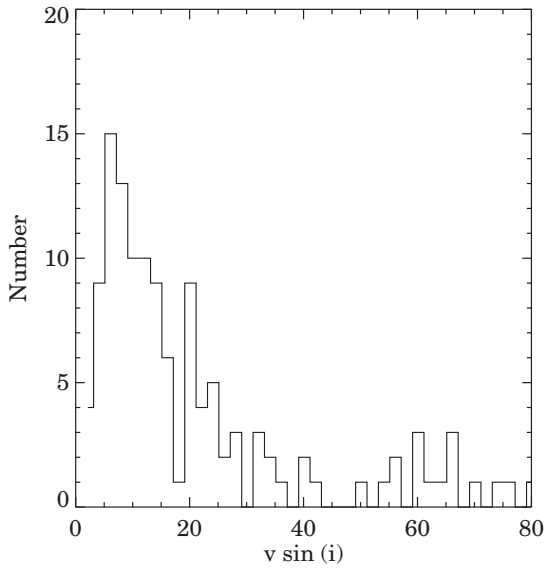

Figure 3. Distribution of derived values of $v \sin i$. As can be seen from the plot, the observed frequency of stars with a particular $v \sin i$ declines at $v \sin i \lesssim 6$ km s^{-1} as a result of an instrumental detection threshold as well as a true lack of stars with very low $v \sin i$.

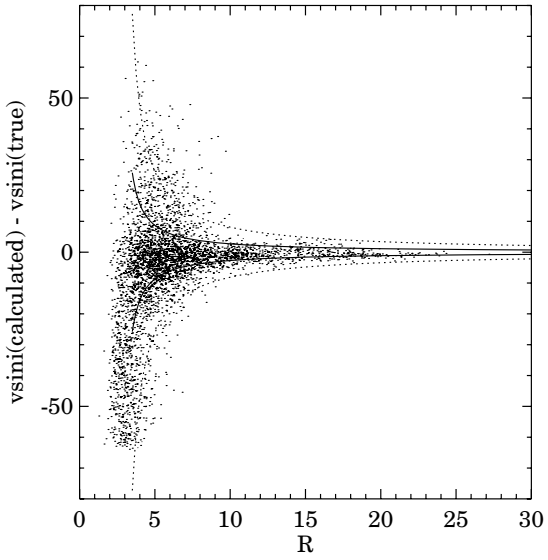

Figure 4. Error in the $v \sin i$ values calculated by our cross-correlation routine as a function of R. Each data point represents a synthetic target that has been rotationally broadened to some $v \sin i$(true) and then correlated against the template grid to find the best matching template. $v \sin i$(calculated) was then determined from the relationship between $v \sin i$ and the width of the correlation function peak. The solid line shows a fit to the 1σ width of the distribution, while the dashed line represents a similar fit to the 3σ width of the distribution (see the text for fit parameters).

analysis revealed that our ability to derive accurate $v \sin i$ values was greater for the cross-correlations performed on the red region. This effect was likely due to the fact that the $C(v_R)$ peaks tended to have a more Gaussian shape for the red cross-correlations. Thus, in future discussions R refers to the value of R calculated for the red region.

The relationship between σ_C and the target $v \sin i$ was calibrated separately for each template spectrum by cross-correlating the template spectra with synthetic target spectra for which $v \sin i$ is known. The synthetic target spectra were created by introducing artificial rotational broadening into the template spectrum and degrading the spectral resolution and sampling to match the Hectochelle data. We performed this test for each template with synthetic targets whose $v \sin i$'s ranged from 0 to 99 km s^{-1} in steps of 3 km s^{-1}. The best-fitting template for the example target spectrum in Figure 1 is also shown in that figure, modified to reflect the corresponding v_R and $v \sin i$ as determined through our cross-correlation procedure.

3.3. Parameters Derived from Cross-Correlation

Once the best matching template spectrum for a target has been found, the target's $v \sin i$ is measured by using the width of the cross-correlation peak as an input for a fifth-order polynomial fit to the σ_C–$v \sin i$ relation previously determined for that template. Valid $v \sin i$ values can only be derived when the σ_C for the target is within the range of σ_C calculated for the template. In total, valid $v \sin i$ values were derived for 489 stars. Figure 3 shows the distribution of $v \sin i$ values for stars in our sample. The absence of stars with $v \sin i \lesssim 6$ km s^{-1} likely represents a combination of a true lack of stars with low $v \sin i$, as well as the resolution limit of the Hectochelle spectrograph (9 km s^{-1}). The finite spectral resolution and standard measurement uncertainties produce cross-correlation widths for low $v \sin i$ stars that are narrower than the minimum σ_C values in the template calibrations. Our inability to separate the instrumental bias from the true statistics at low $v \sin i$ motivated our decision to impose a cutoff in $v \sin i$ (see Section 4.2).

3.4. Uncertainties in $v \sin i$

Rigorous uncertainties were calculated for the $v \sin i$ values derived from the cross-correlation procedure by running a Monte Carlo test on a set of artificial spectra. The synthetic spectra were rotationally broadened to arbitrary $v \sin i$ and then matched to the resolution and sampling of the Hectochelle data. Gaussian noise was also added to the synthetic targets to simulate the effects of a finite signal-to-noise ratio in the actual data. The 1σ amplitude of the noise was one-fourth the mean signal level, characteristic of the lowest quality data in the Hectochelle observations. Since the value of $v \sin i$ is known for the synthetic spectra, the difference between the calculated $v \sin i$ and the true $v \sin i$ for the synthetic spectra provides a measure of the uncertainties inherent in our cross-correlation procedure.

Uncertainties in $v \sin i$ were determined as a function of R for each synthetic target. Figure 4 shows the deviation, $\Delta v \sin i$, between the input and calculated value of $v \sin i$ for each synthetic target as a function of R. As should be expected, $\Delta v \sin i$ decreases with increasing R since higher R corresponds to a better match between the target and template. Following Hartmann et al. (1986), we quantify the $\Delta v \sin i$ versus R relation by fitting a curve of the form $a/(b+R)$ to the 1σ width of $\Delta v \sin i$. We find that the best fit is $\Delta v \sin i = (19.7 \text{ km s}^{-1})/(R - 2.74)$. We apply this relation to the R values measured from actual target spectra to quantize our errors in measured values of $v \sin i$.

4. DISTANCE DETERMINATION

The combination of period, luminosity, effective temperature, and $v \sin i$ data allows us to calculate $\sin i$ for each of the stars in our sample. Since $\sin i$ depends on the absolute luminosities of stars in our sample, the observed distribution of $\sin i$ values is inherently dependent on the assumed cluster distance. We use a Monte Carlo routine to produce model $\sin i$ distributions that assume randomly oriented stellar rotation axes and that

incorporate the effects of observational uncertainties. The distance to NGC 2264 is then constrained by comparing model $\sin i$ distributions to observed distributions with different assumed cluster distances. The distance at which the modeled and observed distributions of $\sin i$ agree is our best-fit distance.

4.1. Calculating $\sin i$

Assuming that the measured period, P, of each star is equal to its rotation period at the equator, we have

$$\sin i = \frac{P \cdot (v \sin i)}{2\pi R}, \quad (2)$$

where R is the stellar radius. P and $v \sin i$ are direct observables, but R must be inferred from each star's luminosity, L, and effective temperature, $T_{\rm eff}$, using the Stefan–Boltzmann relation. L must itself be estimated from each star's extinction-corrected bolometric magnitude ($m_{\rm bol}$) and an adopted distance to the cluster

$$L = 10^{-0.4(m_{\rm bol} - 5 \log D + 5)}. \quad (3)$$

Thus, we can write an expression for $\sin i$ that is explicitly dependent on distance

$$\sin i = \frac{P(v \sin i) T_{\rm eff}^2 \sqrt{\sigma/\pi}}{10^{-0.2(m_{\rm bol} - 5 \log D + 5)}}. \quad (4)$$

Since luminosities were previously calculated by Rebull et al. (2006) assuming a distance $D_0 = 760$ pc, it is convenient to re-write Equation (4) as

$$\sin i = \frac{P(v \sin i) T_{\rm eff}^2 \sqrt{\sigma/\pi}}{\sqrt{L_0}\,(D/D_0)}, \quad (5)$$

where L_0 is the luminosity that has been calculated by Rebull et al. (2006) for the stars in our sample. Equation (5) allows us to calculate the $\sin i$ distribution of stars in NGC 2264 from P, $v \sin i$, $T_{\rm eff}$, and L_0 data, as well as an initial estimate of the cluster distance, D_0.

4.2. Selection of Sample Stars

Beginning with our sample of 923 stars for which we have Hectochelle spectra, we use a series of quality cuts to identify those stars that will allow us to produce an unbiased estimate of the distance to NGC 2264. We first restrict our analysis to the 489 stars for which we are able to measure $v \sin i$ using our cross-correlation routine. We further restrict our sample to those stars with a high likelihood of being bona fide members of NGC 2264. Since the cluster is a coherent kinematic system, imposing a radial velocity cut (10 km s^{-1} $< v_R <$ 30 km s^{-1}; Fűrész et al. 2006) on our spectroscopic sample identifies 273 likely members. Of these, 130 have the ancillary measurements (P, $T_{\rm eff}$, and L_R) necessary to compute $\sin i$.

Rebull et al. (2006) identified a number of stars as likely members of NGC 2264 based on their positions in the sky and their location in color–magnitude space. We add one star to our $\sin i$ sample from the catalog of NGC 2264 cluster members compiled by Rebull et al. (2006); this additional star is the only catalog member without a Hectochelle spectrum but with a previous $v \sin i$ measurement, as well as the other measurements necessary to estimate $\sin i$. Finally, we restrict our sample to the 97 stars with measured $v \sin i$ values larger than 9 km s^{-1}, the minimum velocity resolution of our Hectochelle data. In the discussion that follows, we refer to this final subset of 97 stars as the "distance sample;" for clarity we summarize the steps in its selection in Table 1.

Table 1
Summary of Distance Sample Selection

Sample Subset	Number of Stars
1. Initial set of Fűrész et al. (2006) spectra	923
2. Reliable $v \sin i$ results	489
3. Radial velocity members *w/* $v \sin i$	273
4. Ancillary data for $\sin i$ estimate, radial velocity member & $v \sin i$	130
5. $v \sin i > 9$, ancillary data, and radial velocity member	96 (+1 from Rebull et al. 2006)

Table 2 lists all the data used to calculate $\sin i$ for the 97 stars in the distance sample. The "$L_{\rm bol}$ and $T_{\rm eff}$ source" column identifies the type of reddening correction applied to each star's photometry in estimating its luminosity and temperature; stars with an "S" have individual reddening estimates based on observed spectral types, while stars labeled "P" had photometry corrected assuming the modal extinction derived for cluster members by Rebull et al. (2006). Finally, the star added to the distance sample using the $v \sin i$ measurement cataloged by Rebull et al. (2006) lacks a corresponding $v \sin i$ error estimate: its entry in Table 2 lists "none" in the $v \sin i$ error column.

Figure 5 shows the distribution of spectral types for stars in the distance sample. Most of the stars in the distance sample have spectral types in the range of K4 to M3.

4.3. Error Distributions for Observed Parameters

Observational uncertainties affect the shape of the measured $\sin i$ distribution. In order to obtain a reliable distance estimate, we must account for these uncertainties in our modeled values of $\sin i$. To do this, we first estimate uncertainties in P, $v \sin i$, $T_{\rm eff}$, and L from the observational data; a Monte Carlo simulation is then used to incorporate these error distributions into the modeled value of $\sin i$.

The rotation periods of T Tauri stars can be measured with high precision from their light curves. The errors associated with such measurements are usually on the order of 1%. In some cases, confounding factors such as aliasing in the light curves or the presence of multiple starspots can increase these errors dramatically (e.g., Herbst et al. 2002). However, the number of cases in which these effects occur is typically small. Since the period errors are very small compared to the errors associated with other T Tauri measurements (i.e., luminosity and $T_{\rm eff}$), we simply assume that fractional errors in period are normally distributed with a standard deviation of 1%, characteristic of the typical errors in pre-main-sequence stellar period measurements.

For the remaining variables, it is possible to ascertain some measure of the actual errors from the observed data. Fractional $v \sin i$ errors for the distance sample were calculated using the relationship between R and $\delta(v \sin i)$ given in Section 3.4. The resulting error distribution is consistent with a normal distribution with $\sigma = 20\%$.

Fractional errors in $T_{\rm eff}$ were determined by comparing values of $T_{\rm eff}$ calculated using individual spectral type-based reddening corrections or simply adopting the modal reddening for all cluster members. The $T_{\rm eff}$ error distribution calculated using this prescription is consistent with a normal distribution with

Table 2
Data Used to Create sin *i* Distribution

R.A. (deg)	Decl. (deg)	log L_{bol} (ergs s^{-1})	log T_{eff} (K)	L_{bol} and T_{eff} Source	Period (days)	$v \sin i$ (km s^{-1})	$v \sin i$ Error (km s^{-1})
99.8594131	9.6863384	33.590	3.630	S	5.51	16.5	1.51
99.8765793	9.5604086	33.530	3.640	S	5.49	57.5	6.39
99.9138336	9.9332304	33.420	3.590	S	0.86	66.9	5.33
99.9232178	9.5779305	34.180	3.760	S	3.61	24.6	2.18
99.9446716	9.6816502	34.160	3.740	S	3.84	24.6	2.43
99.9566879	9.5561504	33.470	3.650	S	6.53	10.5	4.08
100.0046692	9.5926476	33.000	3.540	P	9.04	21.6	13.24
100.0111237	9.5900726	33.100	3.540	P	4.65	14.1	28.76
100.0250320	9.8285141	33.160	3.560	S	8.12	13.9	4.70
100.0429306	9.6486139	33.810	3.630	S	3.83	33.9	1.25
100.0453644	9.6686916	32.800	3.540	S	11.73	11.1	25.58
100.0804520	9.8083334	33.540	3.590	S	1.03	62.1	3.60
100.0844803	9.9350996	33.600	3.540	S	3.87	25.7	20.12
100.0988846	9.9232969	33.200	3.530	P	4.57	15.3	27.21
100.1061554	9.8072138	33.620	3.640	S	3.14	25.0	2.20
100.1191101	9.5965662	33.530	3.590	S	4.57	15.8	1.97
100.1206131	9.7047615	33.480	3.620	S	7.22	16.0	1.17
100.1275787	9.7696247	33.600	3.670	S	7.23	12.5	1.07
100.1285858	9.5779390	33.810	3.680	S	12.09	10.5	8.96
100.1318436	9.8064947	33.440	3.640	S	4.17	23.5	1.75
100.1366730	9.8581495	33.580	3.590	S	3.46	30.1	9.57
100.1436234	9.5884171	33.240	3.550	S	3.88	85.9	15.74
100.1521683	9.8460083	33.370	3.550	S	7.79	9.6	5.37
100.1526184	9.8063803	33.470	3.630	S	16.49	11.4	3.64
100.1528091	9.7895918	35.730	3.930	S	4.12	87.9	33.18
100.1550217	9.5194111	33.220	3.550	P	1.15	15.7	5.25
100.1668930	9.5841417	33.680	3.660	S	4.50	13.1	0.95
100.1723404	9.9038496	34.240	3.760	S	3.42	41.2	2.19
100.1806259	9.8498755	33.580	3.630	S	9.04	11.2	1.01
100.1838608	9.3987112	33.490	3.690	S	2.26	37.6	6.33
100.1868820	9.9622917	33.790	3.640	S	16.05	9.1	0.84
100.1876907	9.7616167	33.480	3.630	S	4.61	21.4	2.84
100.1920166	9.8214893	34.790	3.730	S	0.74	75.9	1.51
100.2003937	9.8942642	33.330	3.650	S	5.43	12.7	1.46
100.2011337	9.6107359	33.360	3.550	S	1.67	52.0	9.42
100.2035065	9.7237997	33.110	3.550	P	9.04	15.1	8.61
100.2144318	9.6206837	33.200	3.580	S	8.94	9.1	2.53
100.2194901	9.7391720	33.220	3.550	S	5.41	14.4	3.27
100.2234802	9.5568609	33.620	3.720	S	2.38	27.6	1.23
100.2260971	9.8223219	33.240	3.550	S	9.80	16.2	5.51
100.2481079	9.5863609	34.180	3.630	S	3.35	43.3	2.07
100.2500000	9.4805641	33.560	3.630	S	4.18	22.9	2.29
100.2521362	9.4877644	33.820	3.680	S	5.22	40.9	2.35
100.2532425	9.8562031	34.040	3.710	S	4.41	20.2	1.71
100.2607727	9.5869751	33.490	3.640	S	4.24	17.7	1.42
100.2642822	9.5013723	33.380	3.530	P	1.31	64.4	13.03
100.2645721	9.5217781	34.310	3.760	S	2.18	61.0	2.64
100.2648849	10.0098276	33.220	3.570	S	11.20	12.6	2.56
100.2650299	9.5080585	33.320	3.510	P	9.71	26.1	71.63
100.2668304	9.8191080	33.810	3.670	S	12.43	13.8	1.12
100.2680588	9.8061390	33.780	3.700	S	1.32	20.3	0.96
100.2683716	9.8639193	34.460	3.720	S	3.75	33.7	1.22
100.2707062	9.8461361	33.910	3.700	S	3.70	33.0	1.78
100.2712402	9.8133221	33.430	3.570	S	3.57	16.1	2.80
100.2712479	9.8623857	33.640	3.670	S	9.88	11.1	0.98
100.2723541	9.5537281	33.610	3.640	S	1.20	27.4	2.08
100.2740784	9.8048582	34.030	3.680	S	8.46	13.4	2.94
100.2742157	9.8799639	33.510	3.620	S	4.21	22.3	1.95
100.2758408	9.6063833	34.120	3.720	S	3.00	9.7	1.54
100.2787323	9.4900112	33.240	3.600	S	3.14	10.2	3.91
100.2798233	9.4633245	33.970	3.660	S	9.61	13.4	0.90
100.2802658	9.9753218	33.690	3.650	S	2.59	34.5	2.79
100.2823486	9.6874838	33.490	3.570	S	1.97	20.8	1.87
100.2833862	9.5112028	33.450	3.680	S	3.88	20.5	2.11
100.2868195	9.3952942	33.790	3.600	S	1.83	67.9	2.41

Table 2
(Continued)

R.A. (deg)	Decl. (deg)	log L_{bol} (ergs s^{-1})	log T_{eff} (K)	L_{bol} and T_{eff} Source	Period (days)	$v \sin i$ (km s^{-1})	$v \sin i$ Error (km s^{-1})
100.2873383	9.5627832	33.450	3.530	S	0.80	76.9	92.72
100.2895279	9.8639059	33.680	3.550	S	5.92	67.3	5.20
100.2958221	9.5988054	33.560	3.600	S	11.08	17.5	28.98
100.3050003	9.4362030	34.140	3.670	S	1.76	56.5	2.94
100.3102951	9.5559502	33.590	3.600	S	11.07	9.4	0.84
100.3156281	9.4380083	34.190	3.660	S	6.23	28.8	1.63
100.3199310	9.4583778	33.580	3.660	S	5.20	13.3	2.09
100.3237991	9.4906082	33.750	3.560	S	2.43	60.9	4.54
100.3246765	9.4836388	33.300	3.530	S	2.92	71.8	11.75
100.3246994	9.5602837	33.600	3.610	S	6.51	10.2	3.83
100.3265533	9.6614218	33.300	3.600	S	11.32	54.5	15.99
100.3317947	9.5289888	33.940	3.650	S	2.50	36.1	2.07
100.3356018	9.7598753	33.740	3.710	S	1.30	24.2	4.64
100.3417587	9.7202024	33.540	3.680	S	6.51	10.0	2.67
100.3460236	9.7240610	33.170	3.540	S	0.94	62.5	19.33
100.3625031	9.5036526	33.220	3.570	S	5.08	16.8	5.54
100.3631363	9.5850334	33.840	3.700	S	1.54	86.8	3.38
100.3699265	9.6441221	33.920	3.700	P	5.89	22.1	0.68
100.3816910	9.8091164	33.860	3.700	S	5.06	21.6	1.73
100.3833160	10.0068026	33.480	3.650	S	4.74	16.7	2.25
100.4053726	9.7518587	33.700	3.680	S	4.58	11.5	1.14
100.4280701	9.7157307	33.640	3.620	S	3.93	18.8	1.61
100.4286575	9.4189997	33.130	3.590	P	4.74	10.3	3.97
100.4435120	9.7185698	33.390	3.640	S	4.30	14.9	4.71
100.4502716	9.7120361	34.230	3.750	S	1.19	91.0	2.78
100.4542313	9.6850386	33.510	3.580	S	4.48	15.6	1.89
100.4584656	9.4922886	33.510	3.640	S	3.27	29.1	5.66
100.4644318	9.8951693	33.870	3.720	S	3.70	23.3	1.01
100.4644928	9.7360191	33.200	3.570	S	0.68	9.5	2.99
100.4710388	9.9674664	33.780	3.630	S	0.93	80.8	1.89
100.4714890	9.8465023	33.440	3.630	S	5.77	9.2	2.35
100.4918365	9.7184000	33.560	3.640	S	2.11	21.6	2.49

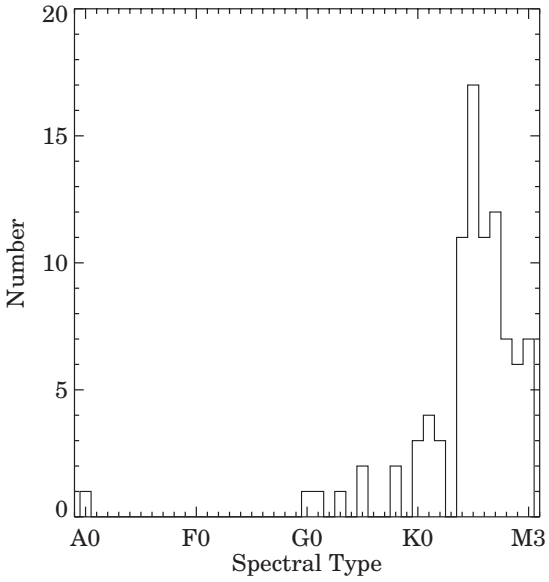

Figure 5. Distribution of spectral types in the distance sample. The bulk of the stars in our sample have types between K4 and M3.

$\sigma = 10\%$. We expect, however, that calculating T_{eff} values by adopting the cluster's modal reddening is less accurate than deriving reddenings from observed spectral types. Indeed, we note a clear relationship between the δT_{eff} value measured for each star and its spectroscopic reddening estimate. This suggests that the difference between the two T_{eff} estimates is dominated by the errors introduced by adopting the modal reddening, and that the resulting error distribution overestimates the actual errors associated with the T_{eff} values derived using individual spectral type-based reddening corrections.

Similarly, the errors in L are estimated from the difference between luminosities calculated assuming a reddening derived from each star's spectral type and those calculated assuming an overall reddening for the cluster. We find that the luminosity error distribution implied by these distinct L estimates lies within the bounds of the normal distribution with $\sigma = 35\%$ suggested by Hartmann (2001) as characteristic of luminosity errors in pre-main-sequence stars.

4.4. Model $\sin i$ *Distributions*

Our technique for modeling the distribution of $\sin i$ in NGC 2264 borrows heavily from Preibisch & Smith (1997). We define the modeled value of $\sin i$, $(\sin i)_m$ as follows:

$$(\sin i)_m = \frac{P_0 (v \sin i)_0 (T_{eff})_0^2 \sqrt{\sigma/\pi}\, S}{\sqrt{L_0}} \times \left[\frac{\frac{P}{P_0} \frac{(v \sin i)}{(v \sin)_0} \frac{T_{eff}^2}{(T_{eff})_0^2}}{\frac{\sqrt{L}}{\sqrt{L_0}}} \right], \quad (6)$$

where the subscripted variables represent the actual values independent of measurement uncertainties, and the non-subscripted

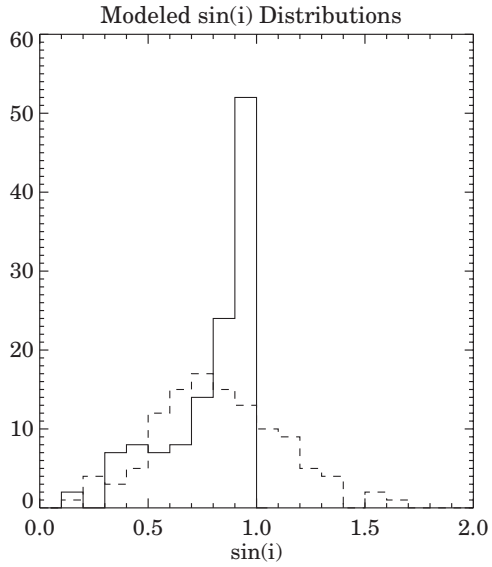

Figure 6. Modeled $\sin i$ distribution assuming random axial orientations before (solid line) and after (dashed line) taking into account measurement uncertainties. The measurement uncertainties assumed in the generation of the model distribution are drawn randomly from the observed uncertainty distributions. We also restrict the model to $v \sin i > 9$ km s^{-1} (see Section 4.4.1).

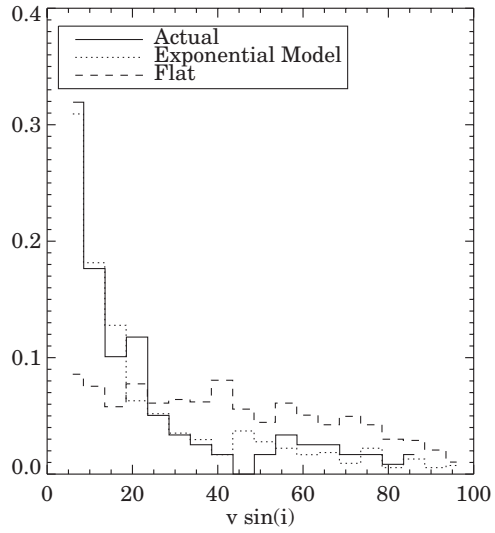

Figure 7. Comparison of the $v \sin i$ distributions resulting from different assumed $v_{\rm true}$ distributions. The exponential model assumes the probability of a star having a particular $v_{\rm true}$ goes as an exponentially decaying function, plus a constant offset. The flat model assumes that all $v_{\rm true}$ in the range considered (0–100 km s^{-1}) are equally likely. As can be seen from the figure, the exponential model fits well to the data.

variables represent the observed values including measurement uncertainties. Equation (6) allows us to split the dependence of $\sin i$ into two parts: the actual value of $\sin i$ (the term outside the brackets) and the contributions of measurement uncertainties (the term inside the brackets).

The $(\sin i)_m$ distribution is generated from Equation (6) using a Monte Carlo routine. Each term of the form X/X_0 (where X represents any of the variables P, $v \sin i$, $T_{\rm eff}$, or L) is calculated by drawing randomly from the appropriate error distribution for our data set, as described in Section 4.3. This process assumes that fractional errors in $v \sin i$, $T_{\rm eff}$, and L are independent of the values of these variables. While this assumption is somewhat questionable, the deviation from the true error distribution is likely small. An example of a $(\sin i)_m$ distribution that includes the effects of observational uncertainties is shown in Figure 6.

4.4.1. Distribution of v_{true}

In order to incorporate the effects of the $v \sin i$ cutoff adopted in Section 4.2 into our model, it is necessary to assume some prescription for the distribution of the true equatorial velocities, $v_{\rm true}$. Once such a prescription has been assumed, modeled $v \sin i$ values can be calculated, allowing the model sample to be restricted in the same manner as the observational sample.

We tested a variety of $v_{\rm true}$ distributions by combining randomly sampled v values with random axial orientations and comparing the resultant set of modeled $v \sin i$ values with the observed $v \sin i$ values. The input $v_{\rm true}$ distribution was adjusted until the sampled population produced a satisfactory match with the observed $v \sin i$ values, as indicated by a two-sided Kolmogorov–Smirnov (KS) test. We find that modeling the $v_{\rm true}$ distribution as an exponentially decaying function with a constant offset ($P(v_{\rm true}) \propto e^{-\alpha \cdot v_{\rm true}} + C$) leads to a good match with the observed $v \sin i$ distribution. Our best matching $v_{\rm true}$ model has $\alpha = 0.09$ and $C = 0.004$. A KS test comparing the resultant modeled $v \sin i$ distribution with the observed distribution yields, on average, a probability of $\sim 95\%$ that our modeled $v \sin i$ distribution comes from the same underlying distribution as the observed $v \sin i$'s. A flat distribution of $v_{\rm true}$, on the other hand, can be rejected with a probability greater than 99.999%. See Figure 7 for a comparison of the assumed $v_{\rm true}$ distributions. This result is in agreement with that found by Jeffries (2007).

4.4.2. The Binary Correction

Some unknown fraction, B, of the stars included in our catalog are unresolved binary systems. For such systems, the value of L that we calculate will characterize the total system luminosity, not the luminosity of a single star. That is, unresolved binaries result in overestimates of the luminosity of the primary star. Since the value of $\sin i$ depends inversely on $\sqrt{L}$, the presence of unresolved binaries in our observational sample will cause $\sin i$ to be systematically underestimated, or conversely, for the value of $(\sin i)_m$ to be systematically overestimated.

To correct $(\sin i)_m$ to account for unresolved binaries, we assume that the masses and luminosities of both the primary and the secondary can be related through a mass–luminosity relation of the form

$$L = kM^a, \tag{7}$$

where k and a are constants. Thus, we can express the total luminosity of the primary and secondary, L_T, as

$$L_T = L_P \left(1 + q^a\right), \tag{8}$$

where L_P is the luminosity of the primary and q is the mass ratio of the secondary to the primary, $q = M_s/M_p \leqslant 1$. Assuming that the temperature derived for the binary system corresponds to the temperature of the primary, then the value of $(\sin i)_m$ calculated for the primary star in a binary system can be corrected by simply dividing by a correction factor of $\sqrt{1+q^a}$. Since we do not know the exact values of q, we simply assume that q is uniformly distributed between 0 and 1. While the true distribution of q is almost certainly not uniform, the deviation from a uniform distribution is likely small enough to not significantly impact our results.

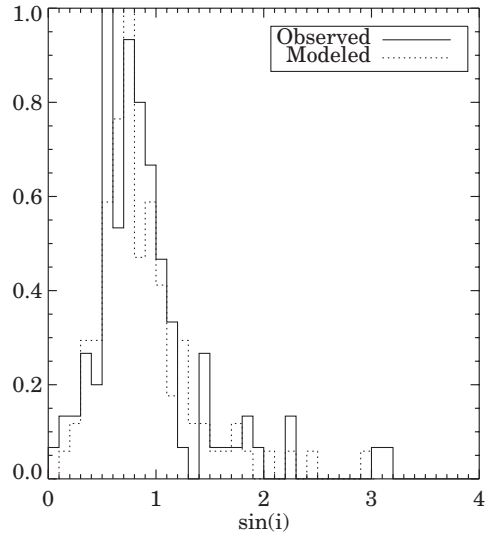

Figure 8. Comparison of the observed distribution of $\sin i$ assuming a distance to NGC 2264 of 913 pc with the modeled distribution.

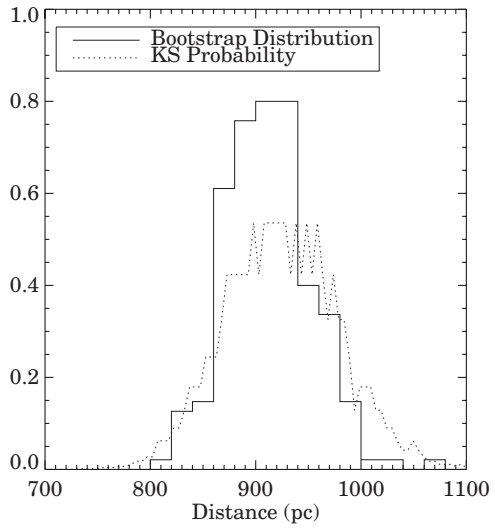

Figure 9. Distribution of bootstrapped best-fit distances is overlaid on a plot of the P_{KS} vs. distance curve for the observed data. A binary fraction of $B = 0.5$ is assumed, and errors are drawn randomly from the observed error distributions.

To determine the value of a in Equation (8), we fit to the mass and luminosity models derived for pre-main-sequence stars between the ages of 1 and 10 Myr by Baraffe et al. (1998). From this fit, we derive a value of $a = 1.5$.

The binary fraction for NGC 2264 is poorly constrained. The multiplicity of nearby main-sequence field stars appears to be mass dependent, ranging from ∼50% for G stars (Duquennoy & Mayor 1991) to ∼30% for M stars (Fischer & Marcy 1992; Reid & Gizis 1997; Delfosse et al. 2004). The multiplicity for regions of isolated star formation, such as Taurus, has been found to be considerably higher than the field population, perhaps larger than 80% (Simon et al. 1993). Clustered regions such as the ONC and NGC 2264, however, show no such excess (Köhler et al. 2006), suggesting initial conditions or dynamical evolution at early ages have an important effect of stellar multiplicity in the pre-main-sequence phase. As NGC 2264 is closer in character to the ONC than Taurus, we assume a value of $B = 0.50$ as the preferred binary fraction for our model, and investigate values as low as $B = 0.0$ and as high as $B = 0.75$.

4.5. Comparing Model $\sin i$ *Distributions with Observations*

4.5.1. Measuring a Best-Fit Distance

We compare the modeled distribution of $\sin i$ to the observed distribution using two-sided KS tests over a range of assumed distances. The KS tests were repeated 100 times at distances of 600–1100 pc in steps of 5 pc. The distance with the highest median KS probability, P_{KS}, is the best-fit distance. Figure 10 shows the P_{KS} versus distance curve for the most likely set of adopted model parameters (solid line: $B = 0.5$, all errors drawn from the observed error distributions). We find the best-fit distance to be 913 pc. At this distance, the median KS probability is ∼ 0.5. The observed and modeled distributions corresponding to this best-fit distance are shown in Figure 8.

4.5.2. Measuring Statistical Errors with a Bootstrap Analysis

We have performed a bootstrap analysis to obtain a rigorous estimate of the statistical uncertainties associated with our measurement of the distance to NGC 2264. In the bootstrap procedure, many artificial $\sin i$ data sets are generated by selecting with replacement from the actual set of observed $\sin i$ values. Each of these synthetic data sets is analyzed using the method described in Section 4.5 to determine a best-fit distance to the cluster. The resultant distribution of derived distances provides an estimate of the true distance, and the width of the distribution provides an estimate for the uncertainty in our derived distance. By using replacement, the bootstrap procedure tests the uncertainty in our distance estimate due to sampling effects, but does not account for any selection effects or biases that would introduce systematic differences between the true and observed $\sin i$ distributions.

For the bootstrap analysis, we generated 200 sets of $\sin i$ values of equal size to the observed sample (i.e., 97 stars) by randomly selecting values with replacement from the list of observed $\sin i$ values. For each of the 200 sets, a best-fit distance was derived using the KS procedure described above. The resultant distribution of distance estimates is shown in Figure 9. We derive a 1σ confidence range for our distance estimate from the width of the velocity region that encloses 67% of the best-fit distances measured with the bootstrap procedure. Combining this uncertainty estimate with the best-fit distance measured in Section 4.5 yields a distance estimate to NGC 2264 of 913 ± 40 pc.

4.5.3. Investigating Systematic Effects

Our distance measurement includes statistical uncertainties due to sampling effects, as calculated above, but also potential systematic errors due to the assumptions that underlie our models. Factors that could introduce systematic errors into our analysis include: the error prescriptions and binary fraction adopted in our calculation of $(\sin i)_m$, the $v \sin i$ cutoff we imposed on our modeled and observed $\sin i$ distributions, biases in the stellar properties derived for stars as a function of their evolutionary state, and finally, the underlying assumption of isotropically distributed rotation axes. We consider in turn the potential impact of each of these effects on our analysis.

The impact of different sources of observational error on the distance determination can be seen in Figure 10, where we compare the P_{KS} versus distance relations produced by comparing our observed sample to models that neglect various components of the $\sin i$ error budget. The solid line represents the case where all of the errors are chosen randomly from the

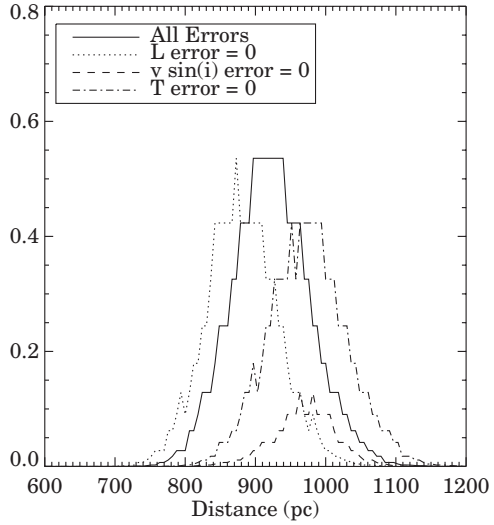

Figure 10. Effect of various assumed error models on the P_{KS} vs. distance curve. Vertical axis represents the probability that the observed sin i distribution at a particular distance was drawn from the same distribution as the modeled sin i distribution.

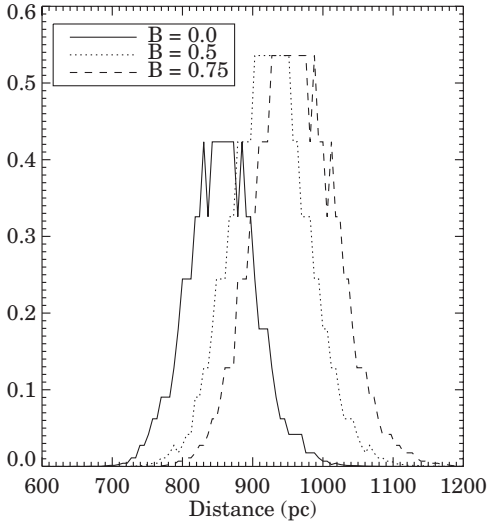

Figure 11. Effect of various assumed binary fractions, B, on the P_{KS} vs. distance curve. Vertical axis represents the probability that the observed sin i distribution at a particular distance was drawn from the same distribution as the modeled sin i distribution.

actual error distributions, and the remaining curves represent cases where the errors in a particular variable have been set to 0. It is clear from Figure 10 that the assumed errors have a non-negligible impact on both the best-fit distance as well as the height of the P_{KS} curve. For instance, negating the luminosity errors has the effect of reducing the best-fit distance by 4%, while eliminating the T_{eff} errors increases the best-fit distance by roughly 6%. Eliminating the $v \sin i$ errors not only increases the best-fit distance by 4%, but also strongly reduces the peak P_{KS}, suggesting that the errors in $v \sin i$ contribute significantly to the shape of the sin i distribution.

To the extent that the error distributions we adopt in our model (see Section 4.3) do not reflect the true error distributions of our data, our distance estimate will be skewed. As shown above, the error distributions we do adopt are influencing our derived distance at the ∼5% level, suggesting any systematic error in our derived distance due to adopting improper error distributions would likely be ∼5% as well. Our error distributions, however, are consistent with those estimated by other authors for the same parameters, and the error distributions push the derived distance in different directions, such that multiple systematic errors should offset one another to some degree. Perhaps most worrisome is the asymmetric shape of the luminosity error distribution, but lacking a more robust means of characterizing the luminosity errors, we are unable to remove this potential systematic effect from our analysis.

Figure 11 shows the effect of the assumed binary fraction on the best-fit distance. As the binary fraction is increased, the average luminosity of the modeled stars is increased, causing the sin i distribution to move to lower sin i as per Equation (6). In order for the observed sin i distribution to remain well matched to the modeled distribution, the assumed distance must therefore increase according to Equation (5). Thus, we see that as the modeled binary fraction changes from $B = 0.0$ to $B = 0.75$, the best-fit distance goes from ∼ 860 pc to ∼ 970 pc, a change of roughly 13%. This is consistent with the results of Jeffries (2007), who found in his ONC study that increasing the binary fraction by 0.2 led to a 4% increase in his modeled best-fit distance.

Biases in the parameters derived for stars in different evolutionary states could also be the results of our analysis. As noted by Jeffries (2007), it may be more difficult to derive accurate temperatures, luminosities, and, thus, radii for classical T Tauri stars (CTTSs) than more evolved weak T Tauri stars; CTTSs typically possess larger extinctions, are irregularly variable, and have significant contributions to their total luminosity from accretion and re-radiation from their circumstellar disk, all of which can complicate the derivation of their intrinsic stellar properties. Following Lada et al. (2006), we identified CTTSs in our sampling using IRAC [3.6–8] colors presented for NGC 2264 members by Texeira et al. (2006) and Texeira (2008); when these CTTSs are excluded from our sample, the best-fit distance to NGC 2264 increases to ∼950 pc. This effect is contrary to that seen by Jeffries (2007), who found a decreased best-fit distance to the ONC once CTTSs were excluded from his sample. Given these contradictory results, and that the effect of removing CTTSs from our sample is comparable to the other systematic effects probed here, we have chosen not to exclude CTTSs from our main analysis.

Our technique assumes that all of the stars in NGC 2264 are at the same distance from Earth. In reality, the cluster has some line-of-sight depth, predicted to be on the order of 28 pc (Dahm 2008). If we assume that the known members of NGC 2264 are biased toward low extinctions, this could cause the distance we derive to the cluster to be slightly smaller than the true geometric center of the cluster. The distance we derive here, however, would properly describe the distance of the population of currently known members; we do not consider this to be a systematic error in our analysis, but rather a nuance that should inform the interpretation of our results.

Finally, the fundamental assumption of random axial orientations is itself somewhat questionable since stellar clusters like NGC 2264 are predicted to have collapsed from single cloud complexes. We might expect, then, for there to be a preferred orientation of stars in the cluster resulting from the conservation of the cloud's initial angular momentum, or possibly from the presence of large-scale magnetic fields. Previous

Table 3
Comparison of Previous Distances Estimates for NGC 2264

Authors	Distance (pc)	Method	Number of Stars
Perez et al. (1987)	950 ± 75	Cluster fitting	21
Neri et al. (1993)	910 ± 50	Cluster fitting	~ 50
Sung et al. (1997)	760 ± 85	Cluster fitting	13
This work	913 ± 40	$\sin i$ statistical technique	97

applications of the $\sin i$ distribution technique have, however, produced results that are in agreement with precise parallax measurements (Preibisch & Smith 1997; Jeffries 2007). This agreement provides evidence in support of the random axial orientation assumption, but it has not been directly confirmed by observations.

The discussion above has revealed a number of potential systematic effects in our analysis. The five potential systematics most amenable to direct investigation (the inclusion of CTTSs in our primary sample; the adopted luminosity, temperature, and $v \sin i$ error distributions; and the assumed binary fraction) all influence the derived best-fit distance at the $\sim 5\%$ level. We therefore combine these individual uncertainties in quadrature to characterize the potential error in our best-fit distance due to systematic effects, producing a estimate of our total systematic uncertainties of $\pm 12\%$, or 110 pc.

4.6. The Derived Distance and Age of NGC 2264

We have calculated distance-dependent $\sin i$ values for a sample of 97 pre-main-sequence stars in the open cluster NGC 2264. By comparing the observed $\sin i$ distribution to a modeled distribution assuming random axial orientations, we derive a distance of 913 pc to NGC 2264; quantitative tests of our analysis reveal sampling and systematic errors of 40 and 110 pc, respectively. Our distance estimate does not rely on evolutionary models to any significant degree.[4]

Our distance estimate is significantly higher than a number of previously determined distances, particularly the widely cited value of 760 pc found by Sung et al. (1997). In general, though, our estimate falls within the typical range of calculated distances (730–950 pc) for NGC 2264. Table 3 provides a comparison of our result to previous distance estimates. A distance to NGC 2264 of 913 pc represents an increase of approximately 20% compared to the widely excepted value of 760 pc, though the two results are formally consistent within the sum of the statistical and systematic error bars.

The mean age of NGC 2264 is commonly cited as ~ 3 Myr, though there is evidence for a considerable age spread within the cluster (Dahm 2008). The luminosities of pre-main-sequence stars are often compared with predictions of theoretical pre-main-sequence models to infer the age of their parent cluster; as luminosity declines through the pre-main-sequence phase, the larger luminosities produced by assuming a greater distance to the cluster will produce a younger inferred age for the cluster. Increasing the assumed distance to NGC 2264 from 760 to 910 pc changes the distance modulus by 0.4 mag. The corresponding 0.4 mag brightening of the stars produces a shift in the age of the cluster. We have produced a crude estimate of the revised age of the cluster by determining the age at which a 1 $M_\odot$ star's H-band magnitude is 0.4 mag brighter than at 3 Myr: according to the pre-main-sequence models calculated by Baraffe et al. (1998), the distance we derive here implies a revised age for NGC 2264 of ~ 1.5 Myr. The detailed analysis of cluster members required for robust estimates of the age and properties of NGC 2264 in light of our new derived distance, however, is beyond the scope of this work.

[4] The one exception is the use of the pre-main-sequence mass–luminosity relation in the derivation of the binary correction factor. This factor had a relatively small effect on our calculated distance, however, and is also well constrained by observations. Thus, our derived distance is almost entirely model independent.

5. CONCLUSIONS

We determined the distance to the open cluster NGC 2264 using a statistical analysis of cluster member inclinations. We derived distance-dependent values of $\sin i$ (where i is the inclination angle) for 97 stars in NGC 2264 from measured rotation periods, luminosities, effective temperatures, and projected equatorial rotation velocities, $v \sin i$, of these stars. We measured 96 of the $v \sin i$ values in our sample by analyzing high-resolution spectra with a cross-correlation technique. We modeled the observed distribution of $\sin i$ for the cluster by assuming that member stars have random axial orientations and by adopting prescriptions for the measurement errors in our sample. By adjusting the distance assumed in the observed $\sin i$ distribution until it matches the modeled distribution, we obtained a best-fit distance for the cluster. We find the data to be consistent with a distance to NGC 2264 of 913 pc. Quantitative tests of our analysis reveal uncertainties of 40 and 110 pc due to sampling and systematic effects, respectively. This distance estimate suggests a revised age for the cluster of ~ 1.5 Myr, although more detailed investigations of the full cluster membership are required to draw strong conclusions.

The authors thank Steve Strom for a prompt and helpful referee report that improved the analysis presented here, and Russel White and Javed Gabor for providing IDL code that formed the basis of our cross-correlation pipeline. E.J.B. acknowledges the support of the SAO Summer Intern Program, made possible by a grant from the NSF. NASA support was provided to K.R.C. for this work through the Spitzer Space Telescope Fellowship Program, through a contract issued by the Jet Propulsion Laboratory, California Institute of Technology under a contract with NASA. A.A.M. was supported by NASA through contract 1335523 issued by JPL/Caltech.

REFERENCES

Anthony-Twarog, B. J. 1982, AJ, 87, 1213
Baraffe, I., Chabrier, G., Allard, F., & Hauschildt, P. H. 1998, A&A, 337, 403
Bessell, M. S. 1991, AJ, 101, 662
Bouvier, J., & Bertout, C. 1989, A&A, 211, 99
Coelho, P., Barbuy, B., Meléndez, J., Schiavon, R. P., & Castilho, B. V. 2005, A&A, 443, 735
Dahm, S. E. 2008, in Handbook of Star Forming Regions, Vol. 1: the Northern Sky, ed. B. Reipurth (San Francisco, CA: ASP), 966
Delfosse, X., et al. 2004, in ASP Conf. Ser. 318, Spectroscopically and Spatially Resolving the Components of the Close Binary Stars, ed. R. W. Hilditch, H. Hensberge, & K. Pavlovski (San Francisco, CA: ASP), 166
Duquennoy, A., & Mayor, M. 1991, A&A, 248, 485
Fischer, D. A., & Marcy, G. W. 1992, ApJ, 396, 178
Flaccomio, E., Micela, G., Sciortino, S., Favata, F., Corbally, C., & Tomaney, A. 1999, A&A, 345, 521
Frasca, A., Biazzo, K., Catalano, S., Marilli, E., Messina, S., & Rodono, M. 2005, A&A, 432, 647
Fűrész, G., et al. 2006, ApJ, 648, 1090
Hartmann, L. 2001, AJ, 121, 1030
Hartmann, L., Hewett, R., Stahler, S., & Mathieu, R. D. 1986, ApJ, 309, 275
Hendry, M. A., O'dell, M. A., & Collier-Cameron, A. 1993, MNRAS, 265, 983
Herbig, G. H. 1954, ApJ, 119, 483

Herbst, W. 1989, AJ, 98, 2268
Herbst, W., Bailer-Jones, C. A. L., Mundt, R., Meisenheimer, K., & Wackermann, R. 2002, A&A, 396, 513
Hillenbrand, L. A. 1997, AJ, 113, 1733
Jeffries, R. D. 2007, MNRAS, 376, 1109
Johns-Krull, C., & Gafford, A. 2002, ApJ, 573, 685
Köhler, R., Petr-Gotzens, M. G., McCaughrean, M. J., Bouvier, J., Duchêne, G., Quirrenbach, A., & Zinnecker, H. 2006, A&A, 458, 461
Lada, C. J., et al. 2006, AJ, 131, 1574
Lamm, M. H., Mundt, R., Bailer-Jones, C. A. L., & Herbst, W. 2005, A&A, 430, 1005
Leggett, S. K. 1992, ApJS, 82, 351
Leggett, S. K., Allard, F., & Hauschildt, P. H. 1998, ApJ, 509, 836
Makidon, R. B., Rebull, L. M., Strom, S. E., Adams, M. T., & Patten, B. M. 2004, AJ, 127, 2228
Mayne, N. J., & Naylor, T. 2008, MNRAS, 386, 261
Neri, L. J., Chavarria-K., C., & de Lara, E. 1993, A&AS, 102, 201
O'Dell, M. A., Hendry, M. A., & Collier Cameron, A. 1994, MNRAS, 268, 181
Park, B.-G., Sung, H., Bessell, M. S., & Kang, Y. H. 2000, AJ, 120, 894
Perez, M. R., Joner, M. D., The, P. S., & Westerlund, B. E. 1989, PASP, 101, 195
Perez, M. R., The, P. S., & Westerlund, B. E. 1987, PASP, 99, 1050
Preibisch, T., & Smith, M. D. 1997, A&A, 322, 825
Rebull, L. M., Stauffer, J. R., Ramirez, S. V., Flaccomio, E., Sciortino, S., Micela, G., Strom, S. E., & Wolff, S. C. 2006, AJ, 131, 2934
Rebull, L. M., et al. 2002, AJ, 123, 1528
Reid, I. N., & Gizis, J. E. 1997, AJ, 113, 2246
Simon, M., Ghez, A. M., & Leinert, C. 1993, ApJ, 408, L33
Strom, K. M., Strom, S. E., & Yost, J. 1971, ApJ, 165, 479
Sung, H., Bessell, M. S., & Lee, S.-W. 1997, AJ, 114, 2644
Szentgyorgyi, A. 2006, New Astron. Rev., 50, 326
Texeira, P. S. 2008, PhD thesis, Univ. of Lisbon
Texeira, P. S., et al. 2006, ApJ, 636, L45
Tonry, J., & Davis, M. 1979, AJ, 84, 1511
Walker, M. F. 1956, ApJ, 124, 668
White, R. J., Gabor, J., & Hillenbrand, L. 2007, AJ, 133, 2524